East Asian summer monsoon simulation by a 20-km mesh AGCM

Akio Kitoh · Shoji Kusunoki

Abstract East Asian summer monsoon climate simulated by a global 20-km mesh atmospheric general circulation model (AGCM) forced by the global sea surface temperature during the period 1979–1998 is investigated. In comparison with a lower resolution (180-km mesh) model experiment, it is revealed that the 20-km mesh AGCM shows the superiority in simulating orographic rainfall not only its location but also its amount. The Baiu frontal structure is also better simulated in the higher resolution model, which leads to stronger Baiu rainfall. The 20-km model also shows more intense extremes in precipitation. Interannual variability of June–August mean precipitation and seasonal march of the monsoon rain band are also investigated.

Keywords East Asian climate · Summer monsoon · High-resolution AGCM · AMIP

1 Introduction

East Asian climate in summer is characterized by the major seasonal rain band, such as Meiyu/Baiu rain band, and typhoons (tropical cyclones). They are influenced by convections over the western Pacific warm pool and the North Pacific subtropical anticyclone. Intermittent appearance of the Okhotsk high also influences the summer climate in this region. El Niño/Southern Oscillation (ENSO) affects the

A. Kitoh (✉) · S. Kusunoki
Meteorological Research Institute,
1-1 Nagamine, Tsukuba, Ibaraki 305-0052, Japan
e-mail: kitoh@mri-jma.go.jp

East Asian monsoon through changes in convection over the western Pacific. Despite continuous model development, atmospheric general circulation models (AGCMs) still have systematic biases in simulating the East Asian summer monsoon such as an underestimation of precipitation amount over the western Pacific (Kang et al. 2002a) and inappropriate temporal characteristics between precipitation and underlying sea surface temperature (SST) (Wang et al. 2005). On the other hand, the horizontal resolution of the model is reported to have positive impact on the simulation of East Asian monsoon (Kobayashi and Sugi 2004; Gao et al. 2006). The spatial scale of the Meiyu/Baiu rain band and tropical cyclones is too small for conventional GCMs to resolve so that the intensity of precipitation is very likely to be underestimated and the probability distribution function of precipitation is distorted at its tail. Therefore, a high spatial resolution model is anticipated for use to study extreme precipitations and to project their modification by climate changes.

Recently, a very high resolution AGCM with the horizontal grid size of about 20 km has been developed (Mizuta et al. 2006), and has been used for climate change projection studies under increasing atmospheric concentrations of greenhouse gases and aerosols (e.g. Kusunoki et al. 2006; Oouchi et al. 2006). The grid size of this model is several times smaller than that previously used in climate model simulations. Kusunoki et al. (2006) showed that the reproducibility of the Baiu rain band in the 20-km model surpasses that in the same model with a lower horizontal resolution. As the 20 km mesh size enables us to give a reasonable representation of the inner structures of a tropical cyclone (Oouchi et al. 2006), the model is able to simulate strong winds and heavy precipitation associated with tropical cyclones. Due to increased horizontal resolutions, orographic rainfall is also well represented (Yata-

gai et al. 2005). As East Asian climate consists of various spatial and temporal time scales, the high-resolution model is now able to simulate meteorological phenomena with large spectrum range.

As the global 20 km model is a unique one in terms of its horizontal resolution as well as its application to long-term integration for global change studies with integration period more than 10 years, it is necessary to fully assess model's performance in its mean climate and interannual variability among others. Although Mizuta et al. (2006) have evaluated a 10-year simulation of this 20-km mesh model integrated with climatological SST assessment of longer model integration with realistic interannually varying SST forcing is needed. We have performed the atmospheric model intercomparison project (AMIP) simulation with this global 20-km mesh AGCM. A parallel simulation with a lower resolution version of the same model (180-km mesh) is also performed. In this paper, we evaluate the East Asian summer monsoon climate and its interannual variations of the global 20-km mesh AGCM in comparison with those of the 180-km mesh AGCM.

The model and experimental setup are introduced in Sect. 2. Mean climate is evaluated in Sect. 3. Reproducibility of interannual precipitation anomalies is investigated by an empirical orthogonal function (EOF) analysis in Sect. 4. The seasonal march of the monsoon rain band is another unique feature of the East Asian monsoon and is discussed in Sect. 5. Finally conclusion is given in Sect. 6.

2 Model and experiment

2.1 Model

The atmospheric GCM used is a next operational global model for short-term numerical weather prediction of Japan Meteorological Agency (JMA) and a part of next generation climate model for long-term climate simulation at Meteorological Research Institute (MRI). The simulations were performed at a triangular truncation 959 with linear Gaussian grid (T_L959) in the horizontal, in which the transform grid uses $1,920 \times 960$ grid cells, corresponding to a grid size of about 20 km. The model has 60 layers in the vertical with the model top at 0.1 hPa. For the cumulus parameterization, the Arakawa-Schubert scheme with prognostic closure (Randall and Pan 1993) is used. Detailed description of the model is given in Mizuta et al. (2006).

Model's performance in the 10-year present-day simulation with climatological SST is described in Mizuta et al. (2006). The simulated precipitation agrees well with the observations in terms of spatial patterns, such as the Intertropical Convergence Zone (ITCZ), the South Pacific Convergence Zone (SPCZ), and Asian summer monsoon

rainy area, but its amount is under-estimated in the western Pacific region and over-estimated around Bay of Bengal and also the eastern Pacific in the JJA season. Model's high horizontal resolution enables us to simulate orographic rainfall such as a maximum to the west of the Western Ghats in southern India and a southern periphery of the Himalaya range (Yatagai et al. 2005).

2.2 Experiment

We have performed AMIP experiments using two different horizontal resolution of the model. One is an original 20-km mesh version of the model, and the other is a reduced resolution experiment. Here we adopted T_L95, which is comparable to T63 and has a grid size of 180 km. This model has 40 layers in the vertical with the model top at 0.4 hPa. At the lower resolutions, the same physical package is used, but the parameter adjustments described in Mizuta et al. (2006) were not included.

Figure 1 shows the topography used in the two versions of the model (cross sections of the topography at 30°N and 15°N appear in Fig. 4). The 180-km resolution depicts a steep rise of the southern flank of the Tibetan plateau and the Tarim Basin with the Tian Shan Mountain to the north, and a hill-like Western Ghats Mountain. Naturally, they are better represented in the 20-km resolution. North–south oriented mountain ranges in the Indochina Peninsula are now well resolved. High mountains over the Indonesian islands also appear only in the higher resolution version.
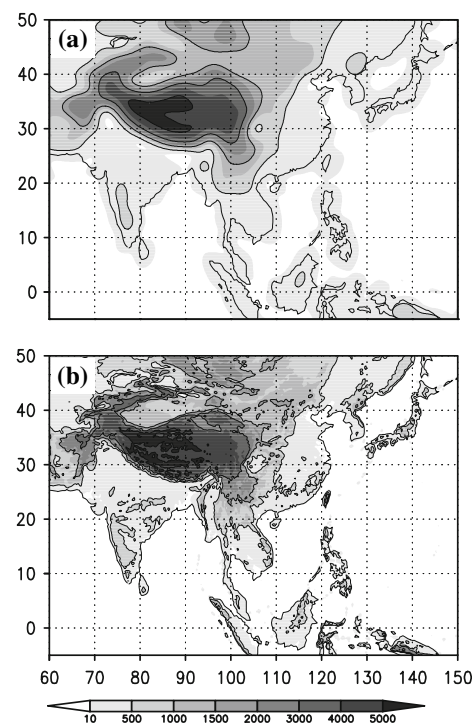

Fig. 1 Topography (meter) in a 180-km model and b 20-km model

Over China, the Sichuan Basin (around 105°E 30°N) and Wuyi Mountain Ranges at the southeastern coast are represented well.

Both models are run for 20 years during 1979–1998 using the observed monthly SST and sea-ice concentration dataset (HadISST, Rayner et al 2003). To assess the statistical significance between the two models' result, three member ensemble runs are performed for the 180-km mesh AGCM with the same boundary conditions but from different initial conditions. Due to computational burden, only one simulation was performed for the 20-km mesh AGCM. In the following, we denote the high resolution run with the 20-km mesh AGCM as 20-km model, and the low resolution run with the 180-km mesh AGCM as 180-km model, respectively. For the 180-km model, the three member ensemble averages are plotted unless otherwise noted.

2.3 Observed data

For model verification we used various precipitation datasets. They are the CPC Merged Analysis of Precipitation (CMAP, Xie and Arkin 1997), the Global Precipitation Climatology Project (GPCP, Huffman et al. 1997, 2001), the gauge-based dataset of daily precipitation over East Asia (Eaclim, Xie et al. 2007) and the Tropical Rainfall Measuring Mission (TRMM) PR3A25 V6 dataset (TRMM 3A25, Iguchi et al. 2000). For the observed climatology, a 20-year (1979–1998) mean for CMAP and GPCP on a 2.5°lat/lon grid, a 20-year (1978–1997) mean for EAclim on a 0.05°lat/lon grid, and an 8-year (1998–2005) mean for TRMM 3A25 on a 0.5°lat/lon grid are calculated.

ERA40 reanalysis dataset (Uppala et al. 2005) is also used for comparison of atmospheric circulation fields.

3 JJA mean climate

First, simulated June–July–August (JJA) mean precipitation climatology for two versions of the model are compared with the various observations in Fig. 2. Both the 180-km and 20-km models capture major convective centers over the eastern Arabian Sea, the Bay of Bengal, the South China Sea and the Philippines Sea, Bangladesh and southwestern part of Japan. Relative low rainfall over the southeastern peninsular India is also well simulated. Compared to the lower resolution version (180-km model), the 20-km model successfully simulates narrow precipitation bands windward of the mountains. There are high rainfalls over the western side of mountains of the Western Ghats, Indochina peninsula, Gulf of Thailand and the Philippines together with lee-wind side precipitation minima. Orographic precipitation along the Himalayas is also seen (Yatagai et al. 2005). The coarser-resolution datasets

(CMAP and GPCP) do not show such a sharp horizontal contrast in precipitation. Simulated rainfall peak is located over the ocean grid point adjacent to the coast, rather than over the land grid point, which is in conjunction with the observed characteristics (Xie et al. 2006). Yatagai et al. (2005) noted that the 10-year MRI 20-km model simulation with the climatological SST reproduces overall precipitation patterns well, but do not include a precipitation maximum that occurs on the southern coast of China during summer. The 180-km model has overestimated precipitation around 100°E, 30°N, which is remedied in the 20-km model. The reproducibility of the Baiu rain band in the 20-km model surpasses that in the same model with a lower horizontal resolution (Kusunoki et al. 2006). These differences between the two models are statistically significant.

In order to quantify the performance of the 20-km model more objectively and rigorously, we introduced the "Taylor diagram" proposed by Taylor (2001), which is widely used in the evaluation of a climate model performance. The root-mean-square (RMS) difference between the observation and model can be decomposed into the bias and the centered pattern RMS difference. Figure 3a shows the RMS differences and biases of models for the JJA mean precipitation climatology. Simulated data by the 20-km and 180-km models are interpolated to the grids point of CMAP and GPCP data with 2.5° spacing. The target domain is the same as that shown in Fig. 2. Here the CMAP data is selected as verification observational data. Skill of GPCP data relative to CMAP data is also plotted for reference of uncertainty of observational estimates. The 20-km model has a smaller bias than the 180 km model, although the RMS difference of the 20 km model is almost comparable to those of the 180-km model.

The centered pattern RMS difference can be regarded as a bias-corrected RMS difference. The Taylor diagram displays a geometric relationship among the centered pattern RMS difference, the observed standard deviation, the simulated standard deviation, and the spatial correlation coefficient. Figure 3b is the Taylor diagram. In this diagram, the radial distance from the origin is proportional to the standard deviation of a simulated pattern normalized by the observed standard deviation. The correlation coefficient between the observed and simulated fields is given by the azimuthal position. The contour shows the measure of skill S, evaluating both the standard deviation and correlation coefficient. S approaches unity in case of a perfect simulation (position of CMAP in the panel). The 20 km model has a slightly larger correlation coefficient than the 180 km model. The standard deviation of the 20 km model is very close to that of CMAP observation. When skill S is used for evaluating both the standard deviation and the correlation coefficient, the 20-km model has a higher accuracy than the

Fig. 2 June–August (JJA)
mean precipitation in mm.
a CMAP, **b** GPCP, **c** EAclim,
d TRMM 3A25, **e** 180-km
model and **f** 20-km model
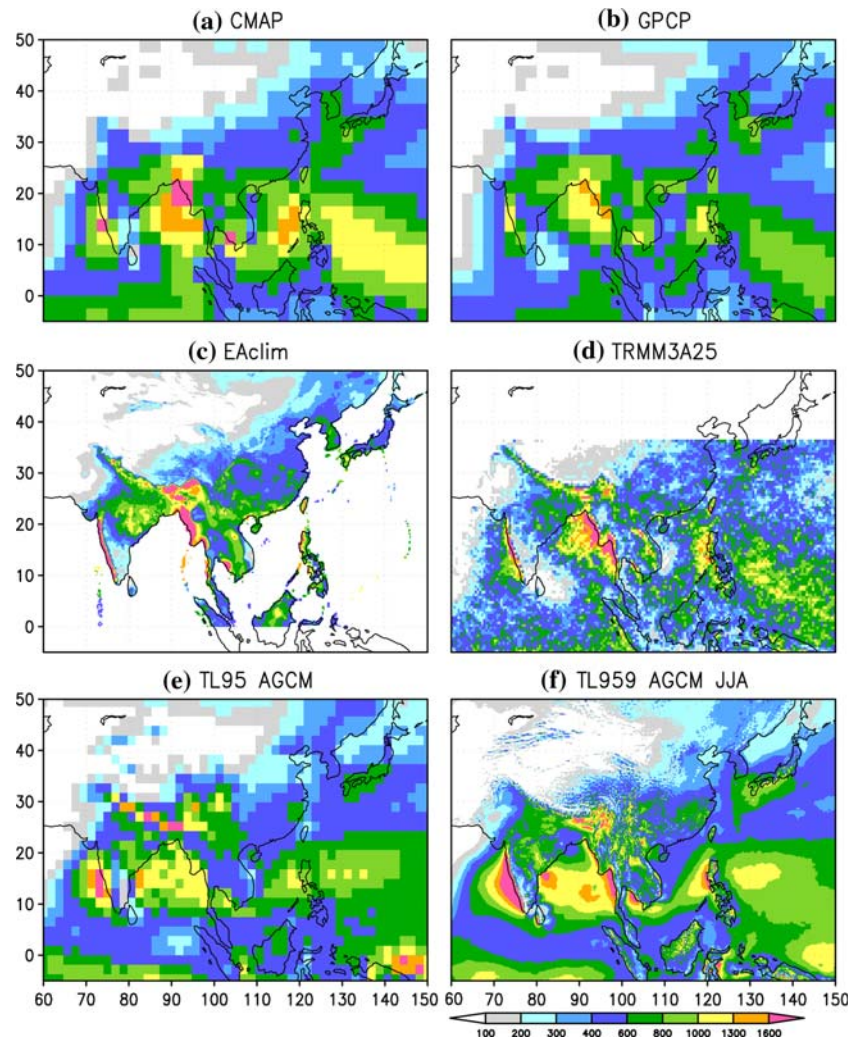
180-km model. Spread of skills among three 180-km model individual runs are small enough to suggest that the difference of skill between the 20-km and 180-km model could be significant in terms of the Taylor diagram.

To see topography-regulated precipitation more clearly, the zonal distribution of JJA mean precipitation along 30°N and 15°N is displayed in Fig. 4. Here the solid black line denotes the 20-km model and the dashed black line the 180-km model, while observations are shown in different colors (red for CMAP, green for GPCP, blue for EAclim and cyan for TRMM 3A25, respectively). Three individual members of the 180-km model are plotted separately to visualize the range of internal variability. They are all averaged over 1° latitude band, that is, 29.5°–30.5°N for 30°N and 14.5°–15.5°N for 15°N. Topography cross-section in each model resolution is also plotted.

At 30°N, all observations except EAclim show a distinct peak of ~950 mm at Kyusyu (130°E), while EAclim shows the largest value of ~1,200 mm. The 20-km model correctly reproduces this peak, while the 180-km model shows

a smoother distribution and underestimates the peak value. By inspecting internal variability of the 180-km model, the significance of this difference is easily depicted in the figure. To the southwestern part of the Tibetan plateau (~75°E), the 180-km model shows the maximum rainfall of ~1,200 mm, while the 20-km model has ~700 mm. The longitudinal peak position differs by 2.5° between CMAP and GPCP, and the peak position in EAcim and TRMM matches well to that in CMAP. The longitudinal peak position in the 20-km model matches well to that in CMAP, EAclim and TRMM, but that in the 180-km model is displaced westward about 3°, which is close to the position in GPCP. The peak values differ more than twice among the observations, and higher resolution data tend to have larger peak values. Toward the eastern edge of the Tibetan plateau, another rainfall peak is located at 102°E. As has been shown in Fig. 3, the 180-km model has overestimated precipitation around 95°E. The 20-km model simulates precipitation of ~600 mm around 110°E and also around 120°E, both of which correspond to local orography. They
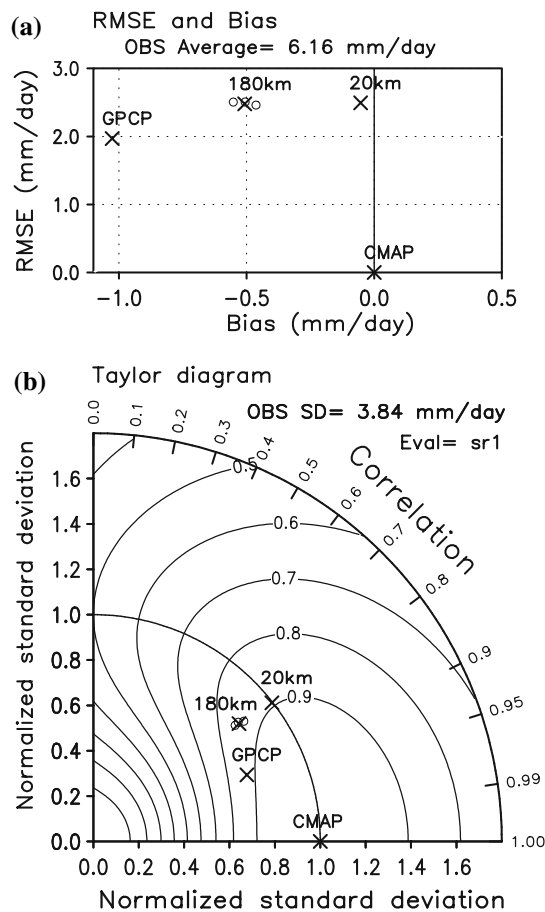
Fig. 3 Skill of geographical distribution of JJA mean precipitation for two models. The CMAP data (Fig. 2a) is selected as verification observational data. The target domain is the same as in Fig. 2 (60°–150°E, 5°S–50°N). Skill of GPCP data (Fig. 2b) relative to CMAP data is also plotted for reference. For 180-km model, the skills of three individual runs and the skill of ensemble average field are shown by *open circles* and by a mark X, respectively. **a** Root mean square error (RMSE) and bias. **b** Taylor diagram for displaying pattern statistics (Taylor 2001). See Appendix of Kusunoki et al. (2006), and Taylor (2001) for technical details

Fig. 4 JJA mean precipitation in mm along **a** 30°N and **b** 15°N. Colors are: CMAP (*red*), GPCP (*green*), EAclim (*blue*), TRMM 3A25 (*cyan*), 180-km model (*black dashed*; three lines correspond to each member) and 20-km model (*black solid*). Topography cross section at each latitude is also shown

are well depicted by EAclim and somewhat by CMAP and GPCP.

At 15°N, the observations show precipitation peaks to the west of the Western Ghats (74°E), to the west of Myanmar (98°E), and to the west of the Philippines (120°E). The 20-km model well reproduces their peak locations and precipitation amount in good comparison to EAclim and TRMM 3A25, although the 20-km model overestimates the peak value to the west of the Western Ghats almost twice the observations. The lower resolution data (CMAP and GPCP) and the 180-km model do not show those peaks well. Overall, these examples clearly show the superiority of the high-resolution model to simulate orographic rainfall not only its location but also its amount.
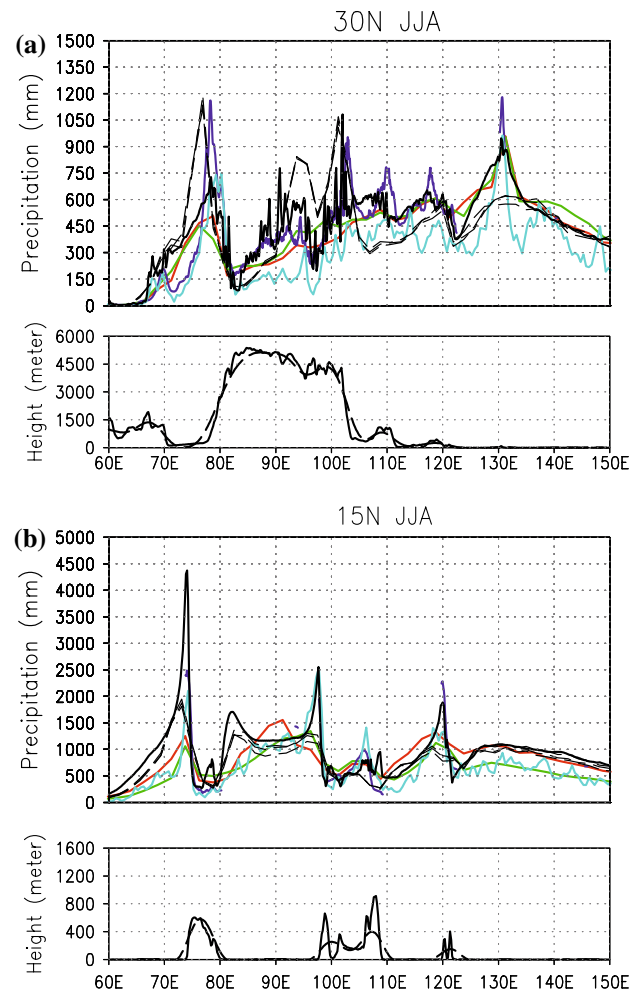
The two models also differ in their simulation of moisture flux fields. Figure 5 displays the vertically integrated JJA mean moisture flux and their divergence fields for the ERA40 data and the two models. The mean sea-level pressure is also contoured. An overall moisture flux circulation field in the two model simulations is in accord with the observed features with westerly fluxes over the North Indian Ocean and easterly fluxes over the tropical and subtropical Pacific Ocean, converging around the Philippines, and then flowing northeastward towards Japan along the western periphery of the subtropical anticyclone in the North Pacific. As shown in Fig. 5d that plotted the differences of moisture flux between the two models where statistically significant, the westerly moisture flux over the Indian Ocean and the South China Sea and the easterly moisture flux over the western tropical Pacific Ocean in the 180-km model are statistically weaker than those in the 20-km model. As such,
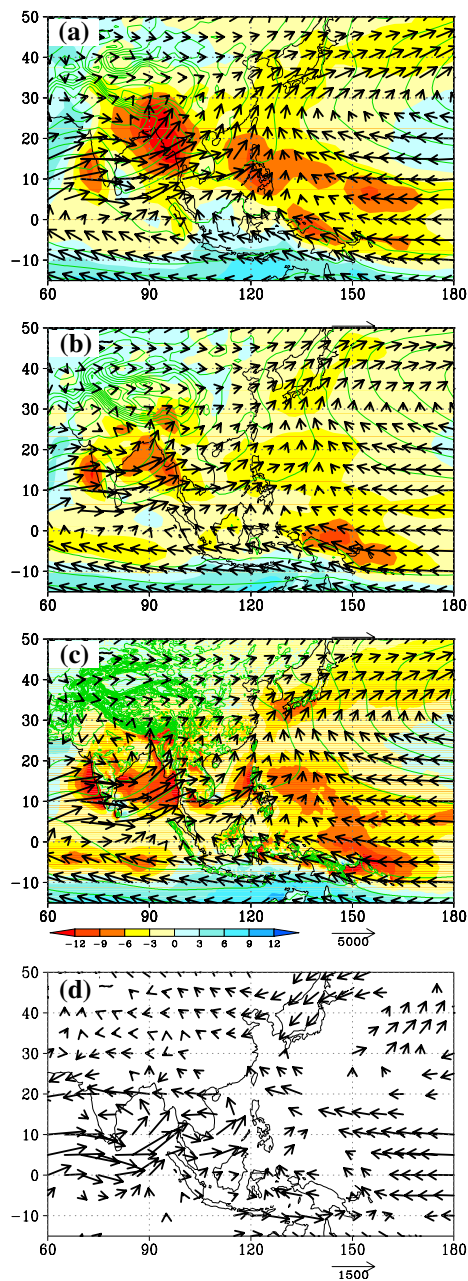
Fig. 5 JJA mean total moisture flux (vector; kg m^{-3}), moisture flux divergence (shade; mm day^{-1}) and mean sea-level pressure (contour; 2 hPa) for **a** ERA40 data, **b** 180-km model and **c** 20-km model. **d** Differences of JJA mean total moisture flux between the 20-km model and the 180-km model. Only the grid points where the difference of either zonal or meridional moisture flux component is statistically significant at 95% level are plotted

the moisture flux convergence around the Philippines in the 180-km model is smaller than that in the 20-km model, while the latter is in good agreement with the observation. Another difference between the two models is that there is a clear contrast in moisture flux divergence/convergence between the land and the ocean in the 20-km model, while they are diffuse in the 180-km model.

The moisture flux consists of wind velocity and atmospheric moisture content. The JJA mean westerly winds in the lower troposphere (e.g. 850 hPa) in the 180-km model are weaker than those in the 20-km model to the west of 120°E, and the trade winds in the 180-km model are weaker than those in the 20-km model to the east of 150°E. Specific humidity in the lower troposphere in the 180-km model is also drier than that in the 20-km model over a large domain from the Philippines Sea and South Asia (not shown). Thus, both the weaker wind velocity and smaller moisture content in the 180-km model contributed to the model's dry bias. The reason of better performance due to higher horizontal resolution is, however, not clear.

The Baiu rain band is one of most distinct characteristics in the East Asian summer climate, making June the wettest month in the western part of Japan. The Baiu front is characterized with a large meridional moisture gradient, and there is a large moisture flux convergence within the Baiu front. The broad-scale Baiu front structure can be reproduced rather well even in a low resolution coupled atmosphere-ocean GCM with 280-km (T42) atmospheric resolution (Kitoh 2004), but Kusunoki et al. (2006) demonstrated that the MRI 20-km model with the climatological SST generally exhibits higher performance in terms of rainfall pattern than lower horizontal resolution versions. Here we compare the Baiu front structure in terms of the latitude-height cross sections of zonal, meridional, and vertical winds and equivalent potential temperature in June at 130°E among the observations based on ERA40 (Fig. 6), the 180-km model (Fig. 7) and the 20-km model (Fig. 8). Statistical significance between the 180-km and 20-km model is calculated and displayed in Fig. 8 by vertical lines.

The observations show the subtropical jet core of 35 m s^{-1} at 35°N, 200 hPa, which extends down to a low-level wind maximum at 27.5°N, 850 hPa. Near the surface, a strong southerly wind component (>4.5 m s^{-1}) is found at 25°N just to the south of the Baiu rain band. An intense upward motion (–0.09 hPa s^{-1} at 30°N, 500 hPa) is seen in the mid-troposphere at the Baiu rain band latitude where a near moist-neutral vertical stratification is also seen. These structures are similar to the well-known structure (Ninomiya 2000). The models basically reproduce main characteristics noted above. However, comparing the 180-km model and the 20-km model, one notes a significant difference in an intensity of the vertical motions around 30°N. The 180-km model shows much weaker upward motion with about 60% strength of the observation. The 20-km model better agrees with the observed strength of about 15% weaker upward motion. The magnitude of the subtropical jet is comparable between the two models, but a southward and downward extension of the jet core is better simulated in the 20-km model. The meridional wind maxima at 25°N, 925 hPa and 35°N, 250 hPa in the 20-km

Fig. 6 Latitude-height cross-sections of June climatology at 130°E based on ERA40 data.
a Zonal wind (m s^{-1}),
b meridional wind (m s^{-1}),
c vertical p velocity Pa s^{-1}, and
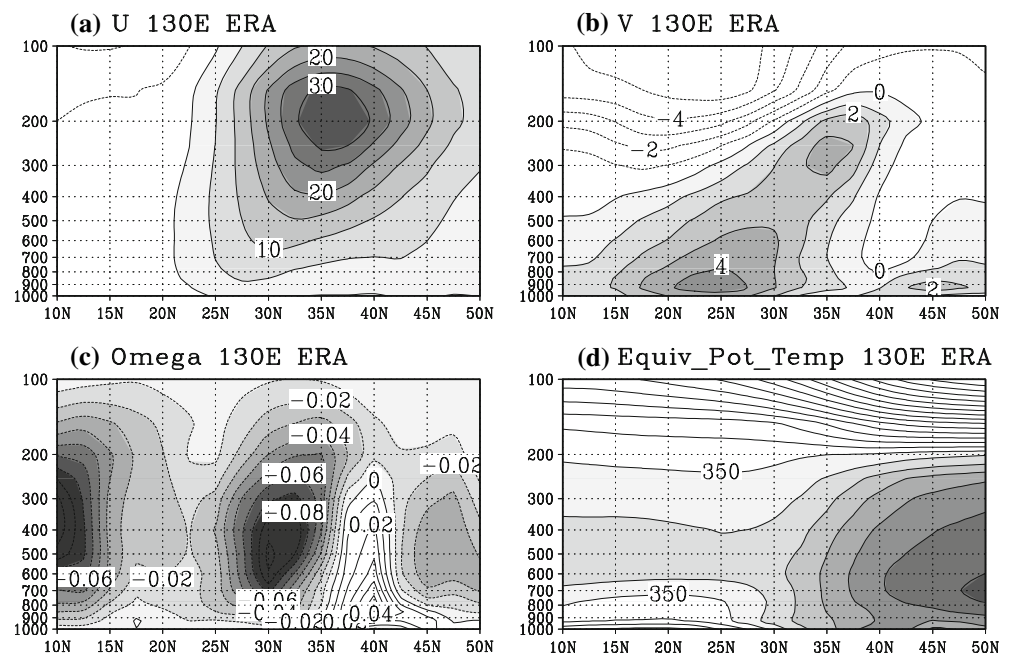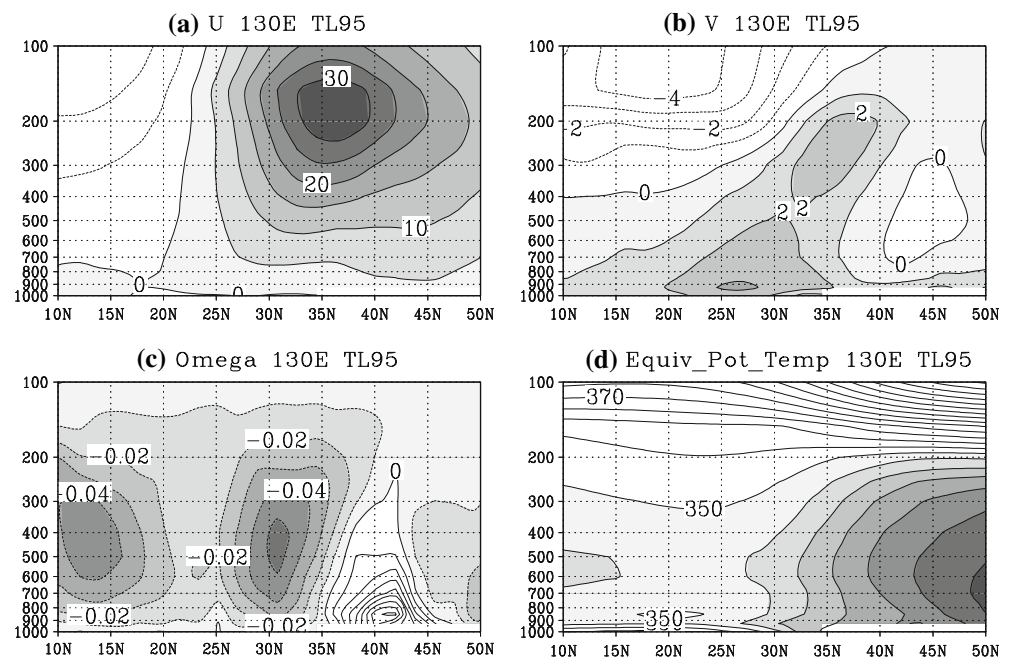**d** equivalent potential temperature (K)

(a) U 130E ERA

(b) V 130E ERA

(c) Omega 130E ERA

(d) Equiv_Pot_Temp 130E ERA

Fig. 7 As in Fig. 6, except for 180-km model

(a) U 130E TL95

(b) V 130E TL95

**(c)** Omega 130E TL95

(d) Equiv_Pot_Temp 130E TL95

model are, however, weaker than the observed, while those in the 180-km model agree better to the observed (these differences between the two models are not significant). Existence of northerly winds to the north of 40°N is well reproduced in the 20-km model. Structure of the equivalent potential temperature is comparable between the two models, but as indicated by vertical lines of statistically significant differences, the equivalent potential temperature in the 180-km model is cooler in the mid-troposphere (about 1°C) than in the 20-km model. Overall, the Baiu frontal

structure is better in the higher resolution model, which is associated with a stronger Baiu rainfall (Figs. 2, 5).

Extreme precipitation events such as heavy rain lead to floods and threaten human life in densely populated Asian countries. The representation of the extremes in precipitation is greatly affected by model's horizontal resolution. Kamiguchi et al. (2006) evaluated precipitation-based extremes indices of the MRI 20-km model run under the present-day condition with the climatological SST, and projected their future changes due to global warming. They

Fig. 8 As in Fig. 6, except for 20-km model. *Vertical lines* denote the region where the difference between the 20-km model and the 180-km model is statistically significant at 95% level
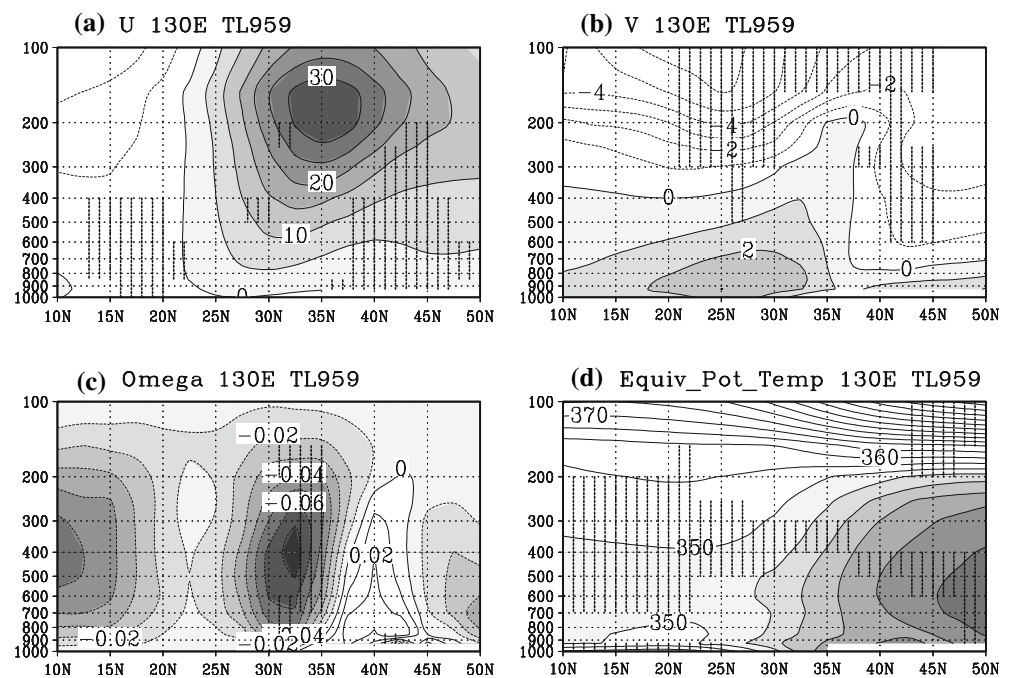
revealed that the model has simulated the horizontal distribution of extremes indices over land in good agreement with those from the observation based on GPCP-1DD (Huffman et al. 2001), but underestimated the magnitude of extremes indices for heavy precipitation somewhat in East Asia, South Asia and Southeast Asia.

As an example of the extremes indices for precipitation, we show the distribution of maximum 5-day precipitation total (R5d) based on 7-year GPCP 1° daily precipitation (1997–2003) in Fig. 9a. R5d is calculated for each calendar year and then averaged for the entire period of data available. Figure 9b, c show R5d in the 180-km model and the 20-km model, respectively, based on the 20-year daily precipitation. Here we used daily precipitation data from one member by the 180-km model. Differences between the two models are shown in Fig. 9d, which is calculated after the model data is interpolated in a common 2° × 2° grid box. R5d in GPCP 1DD data shows regions exceeding 400 mm over the South China Sea and the Philippines Sea. Regions with R5d more than 300 mm cover extensive areas of the above two oceanic areas, and extend to Ryukyu Islands to western Japan and Korea. The 180-km model shows some resemblance of the observed R5d distribution, but underestimates its magnitude over the western Pacific, in particular over East Asia. On the other hand, the 20-km model exhibits much larger R5d values over the South China Sea, the Philippines Sea and the region from Taiwan, Ryukyu Islands to western Japan. A part of the difference comes from more active Baiu rain band in early summer season (Kusunoki et al. 2006), and another from more reasonable representation of tropical cyclones and

associated heavy precipitation bands in the higher resolution model (Oouchi et al. 2006).

It should be noted here about the difference in R5d between the GPCP data and the 20-km mesh model. The difference mainly comes from the data resolution, that is, 1° of the GPCP data versus 0.1875° in the 20-km model. When the 20-km (0.1875°) mesh data is averaged in 1° or 180-km mesh first, and then R5d is calculated, resultant R5d becomes smaller, showing importance of resolution for the extremes indices in precipitation (Kamiguchi et al. 2006). Therefore, we need further investigation on the evaluation of the extreme values.

4 Interannual variability

There is a long history to investigate reproducibility of interannual variations of atmospheric circulation and precipitation fields with an atmospheric GCM forced by the observed interannually varying SST (e.g. Lau 1985). It is generally conceived that models have difficulty to reproduce the interannual precipitation variations outside of the tropics. For example, using the 32 AMIP simulations, Sperber and Palmer (1996) demonstrated that the models forced by the observed global SST captured the interannual variations of Nordeste (Northeast Brazil) precipitation but were less successful in simulating the precipitation variations over India and the Sahel. For the Asian–Australian monsoon region, Kang et al. (2002b) compared 11 AGCMs in simulating atmospheric anomalies during the 1997/1998 El Niño period. Ensemble mean of 10 realizations show
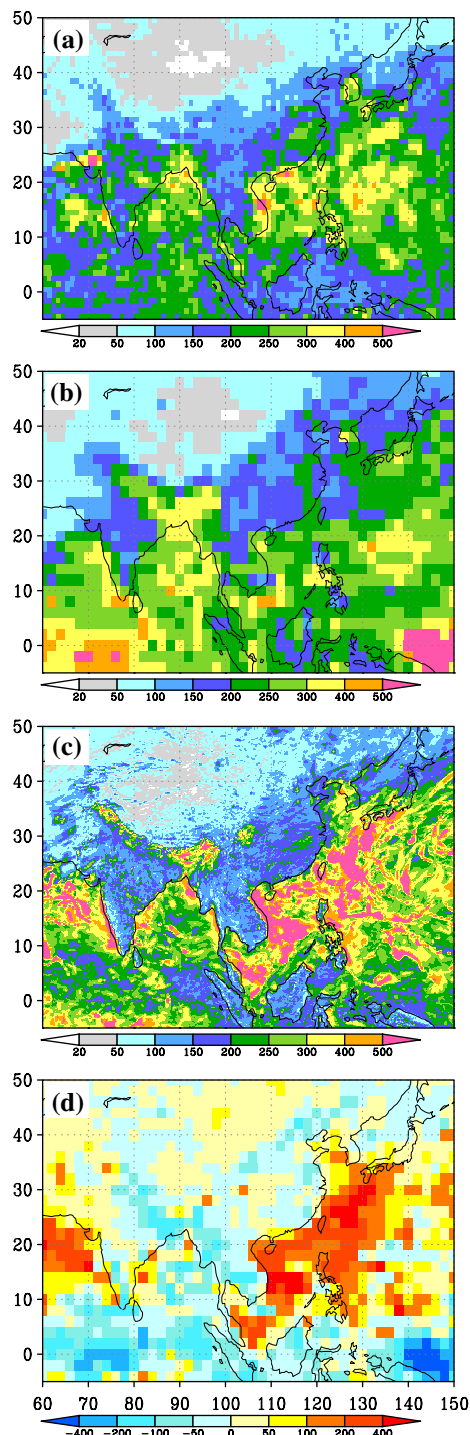
Fig. 9 Maximum 5-day precipitation total (mm) for **a** GPCP, **b** 180-km model and **c** 20-km model. Maximum is calculated for 7 years in GPCP and for 20 years in GCMs. **d** Difference between 20-km and 180-km models interpolated in a common 2° × 2° grid box

El Niño. Wang et al. (2005) noted that the AGCMs, when forced by observed SST, are unable to simulate summer monsoon precipitation anomalies over the Asian-Pacific monsoon region, primarily due to a lack of air–sea interactions. Kitoh and Arakawa (1999) and Wu and Kirtman (2005) have pointed out important role of air–sea interactions in regulating rainfall anomalies over the Asian-Pacific summer monsoon region.

Interannual variations in these AMIP-type simulations consist of the internal mode and the forced mode. When comparing with the observations, the latter forced mode is assessed. The forced mode can be separated from the internal mode using ensemble simulations (Rowell 1998; Sugi et al. 1997), but the computational cost of the global 20-km mesh model inhibits us a calculation of multi-member ensemble runs. Albeit above reservations, it would be interesting here whether the high-resolution model would produce different response in terms of interannual rainfall variations associated with forced SST anomalies.

Figure 10 shows the leading and the second eigenvectors of JJA mean precipitation during the period 1979–1998 in the broader tropics covering 40°S–40°N and their time-series. The JJA mean precipitation for GPCP, the 180-km and 20-km models are first interpolated on a common 1° × 1° grid box, and then an EOF analysis is applied. For the 180-km model, an EOF analysis is performed with each member, and then the three-member ensemble mean is plotted.

The leading EOF for the observed precipitation explains 22.4% of the total variance, and has an equatorial precipitation in the Pacific with opposite polarity over the Maritime Continent, Central America, tropical South America and tropical Atlantic Oceans. This mode seems to be associated with ENSO because its time-series has large negative values in El Niño years 1982, 1983, 1987 and 1997. The observed second mode explains 12.4% of the total variance and is characterized with precipitation contrast between the central to eastern equatorial Pacific and the western subtropical Pacific. This mode may be originated from the SST anomalies over the Indian Ocean and the western tropical Pacific. Both the models reproduce well the time-series, but the 20-km model has slightly larger temporal correlation coefficients (0.85, 0.85 and 0.87 in the 180-km model and 0.91 in the 20-km model for EOF1; 0.64, 0.78 and 0.61 in the 180-km model and 0.82 in the 20-km model for EOF2).

In terms of the spatial distribution of precipitation anomalies, both the models reproduce well the major characteristics of both EOF1 and EOF2 signals over the equatorial Pacific, the Maritime Continent, Central America and the equatorial Atlantic Ocean and the Nordeste, but have less skill in other regions. Spatial correlation coefficients between the observation and the models are 0.31,

that all of the models simulate the spatial pattern of the observed precipitation anomalies reasonably well in the tropical central Pacific with a variety in their amplitudes, however, most of the models had difficulty in simulating the negative anomalies over the Maritime Continent during

Fig. 10 EOF analyses of JJA mean precipitation in the tropics (0°–360°E, 40°S–40°N) for the period 1979–1998. **a–d** EOF1, **e–h** EOF2. **a, e** GPCP, **b, f** 180-km model, **c, g** 20-km model. **d, h** EOF coefficients for GPCP (*thin solid*), 180-km model (*thick dashed*) and 20-km model (*thick solid*)
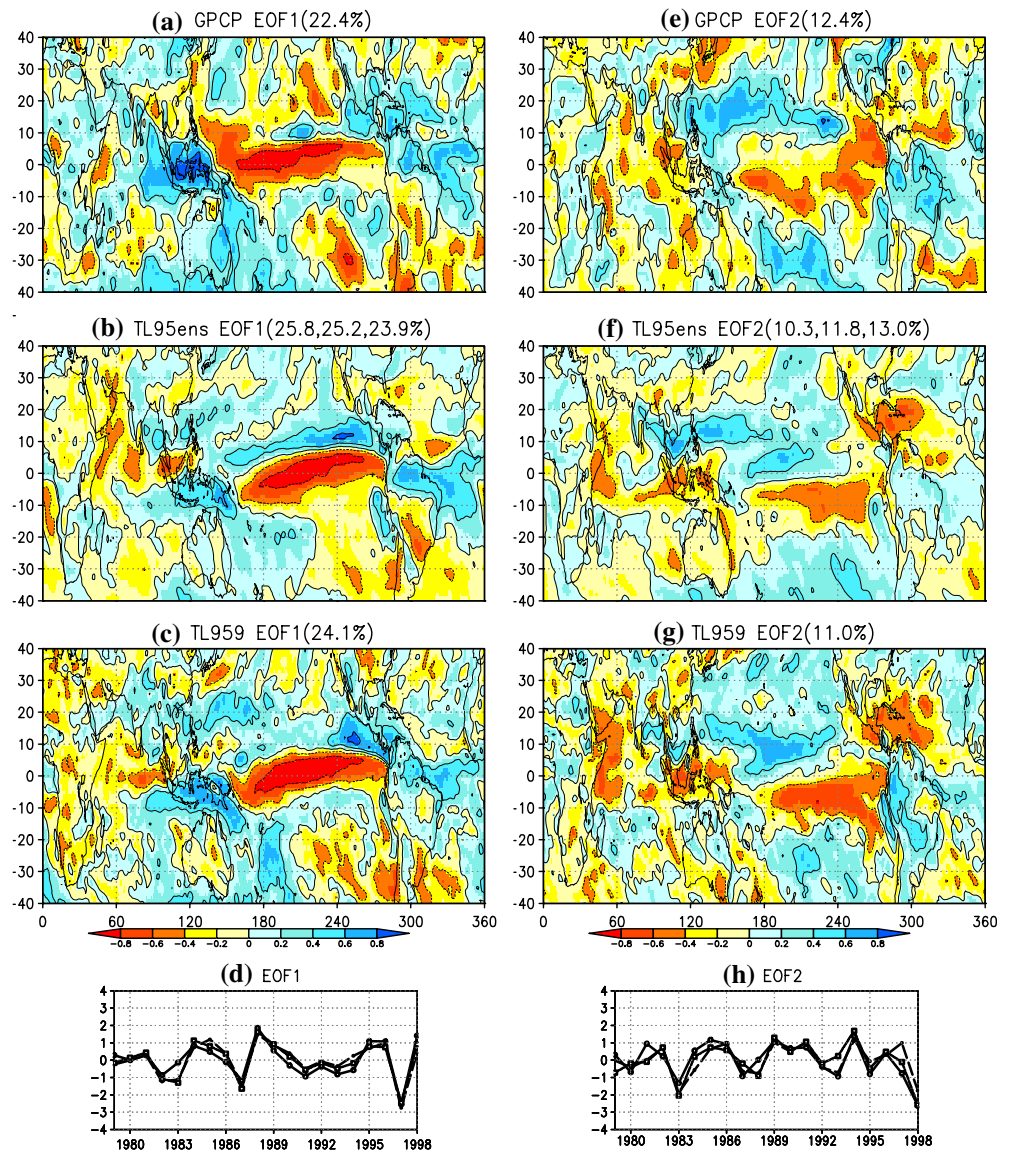
0.38 and 0.35 for each member of the 180-km model (0.40 for the ensemble mean) and 0.46 for the 20-km model for EOF1, while they are 0.27, 0.36 and 0.31 for the 180-km model (0.38 for ensemble mean) and 0.37 for the 20-km model for EOF2. Based on a moderate estimate of degrees of freedom of at least 30, the 20-km model shows better skill in reproducing interannual variability in the precipitation over the broader tropics than the 180-km model does for EOF1. One of notable discrepancy between the observation and the models is the polarity of precipitation anomalies in EOF1 over the Philippines Sea, where the observation reveals the same polarity with that over the equatorial Pacific while the 180-km shows the opposing polarity. The 180-km model shows false precipitation anomalies around 10°N over the ITCZ region. However, this model bias in the EOF1 over the western and the central tropical Pacific becomes less in the 20-km model. A

better precipitation climatology around the ITCZ in the 20-km model than the 180-km model may have resulted in less model error in the EOF1 precipitation pattern, but improvement is not so large. It should be noted that an opposing polarity in the simulated precipitation anomalies in the western Pacific to that observed may be understood as the model's one-way response to local SST anomalies (Wang et al. 2005), and the horizontal resolution can not cure the problem.

5 Seasonal march

The seasonal march of the monsoon rain band is a unique feature of the East Asian monsoon, which is distinct with an abrupt northward advance in early summer (e.g. Ding and Sikka 2006). Its association with spring persistent rains

Fig. 11 Time-latitude cross-section of the 5-day mean precipitation (mm day^{-1}) climatology averaged between 100° and 140°E. **a** CMAP, **b** GPCP, **c** 180-km model and **d** 20-km model. In **d**, *dots* denote the region where the difference between the 20-km model and the 180-km model is statistically significant at 95% level
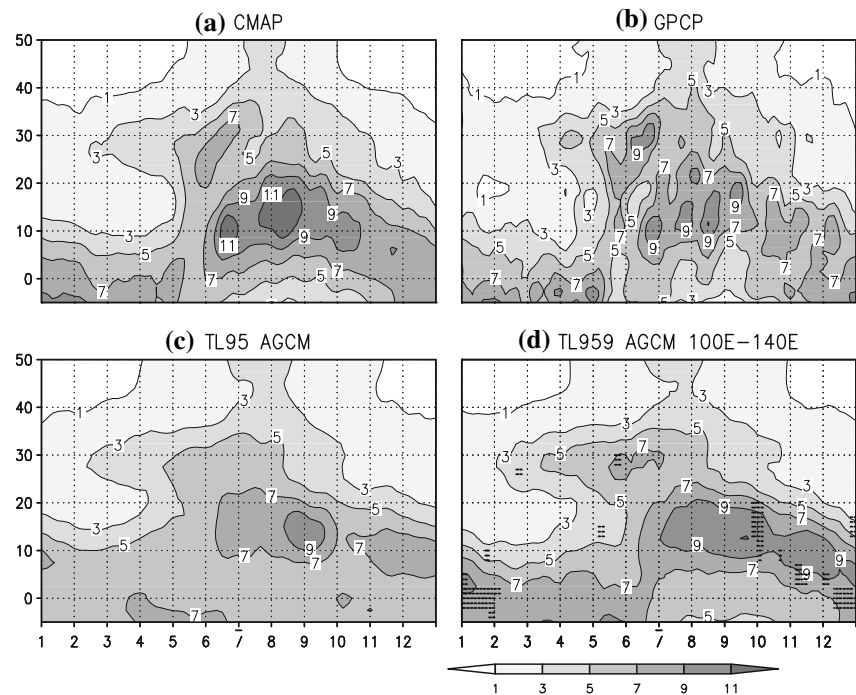
over central China is discussed by Tian and Yasunari (1998). Figure 11a, b illustrate the time-latitude cross sections of 5-day mean precipitation in East Asia by the two observed datasets. Here the longitudinal averages are taken between 100°E and 140°E to capture broad characteristics of Meiyu/Baiu rain band.

In March and April, the CMAP and GPCP data show the persistent rain between 25°N and 30°N, whereas there are relatively dry area between 10°N and 20°N. In early May, there is a sudden increase of precipitation in this latitude, followed by a northward advance of heavy rain area in late May and early June with a maximum rain at 30°N in June (Ueda et al. 1995). Starting from late June throughout summer until September, heavy rain appears in the tropics around the Philippines (10°N–20°N). It is noted that relative magnitudes of the Meiyu/Baiu rain band and the tropical rains in mid-summer differ between the CMAP and the GPCP, in which the GPCP data shows comparable magnitude but the CMAP data show larger precipitation in the tropics. In winter, the CMAP and GPCP data show heavy rains in the tropics.

Both the 180-km model (Fig. 11c) and the 20-km model (Fig. 11d) simulate salient characteristics of the spring persistent rain around 30°N, the summer heavy rain over the Philippines Sea, and the winter heavy rain in the tropics. However, the representation of the Meiyu/Baiu rain band during May and June is different between the 180-km model and the 20-km model. The 180-km model does not reveal a clear maximum in the Meiyu/Baiu rain band, while the 20-km model clearly shows the maximum around 30°N

in May and June. On the other hand, a northward migration of the rain band is not so clear even in the 20-km model compared to the observations. Therefore, further improvements are needed in the seasonal march in precipitation particularly in the western tropical Pacific region, for which some studies suggest that the air–sea interaction should be important and an indispensable player (Ueda and Yasunari 1996).

6 Concluding remarks

We have assessed the performance of a global 20-km mesh AGCM to simulate the East Asian summer monsoon climate by the AMIP experiment for the period 1979–1998, in comparison with its lower resolution version. The 20-km model has been developed by MRI and JMA (Mizuta et al. 2006), will be used for numerical weather forecasting in the operational center (JMA), is capable to reproduce topical cyclones structure and their climatology (Oouchi et al. 2006) and also is durable for long-term integration for the global warming simulation (Kusunoki et al. 2006). Due to its high horizontal resolution, the 20-km mesh AGCM captures orographic rainfall not only its location but also its amount. A comparison with the AMIP experiment with the lower resolution version of the model (180-km mesh) revealed a superiority of the 20-km mesh AGCM in simulating the seasonal mean climate. A hierarchy of phenomena with various spatial as well as temporal scales makes up the climate; the better representation of the high-

resolution model in small-scale features such as Baiu rain band and tropical cyclones resulted in an overall better skill for seasonal mean climate simulation with the 20-km mesh AGCM. An empirical orthogonal function analysis of the interannual June–August mean precipitation also shows an overall better skill in the 20-km mesh AGCM than that in the lower resolution model, which may be associated with a better simulation of mean climatology. Of course, a theoretical limitation for applying an AGCM to the AMIP-type experiment and investigation for predictability of interannual variations should be borne in mind with respect to absence of air–sea interaction (Wang et al. 2005). Absence of air–sea interaction may have resulted in overestimation of extreme precipitation values (Kitoh and Arakawa 1999). Thus, application of this 20-km mesh AGCM in a coupled mode would be a promising next step in the modeling community.

We showed only one example for the heavy precipitation index, i.e., the maximum 5-day precipitation total, for which the lower resolution model has underestimated the intensity of heavy precipitation solely due to resolution problem. Our preliminary work has shown that the 20-km model is suitable for the representation of various extremes indices for temperature and precipitation (Uchiyama et al. 2006; Kamiguchi et al. 2006). The relative importance of resolution issue may differ on the nature of respective extremes indices. The tropical cyclones are now well simulated in the model than in previously reported lower resolution models, though not yet sufficient compared to cloud resolving model with a mesh size of a few kilometers or finer. An impact assessment study in a global scale with this 20-km mesh model becomes possible, and we have started such a work targeting various regions of the world.

In this paper, we concentrated our discussion on the East Asian summer monsoon climate. The performance of the Asian winter monsoon and its interannual variability as well as monsoons in other regions in this MRI 20-km model AMIP simulation will be elaborated in a future work.

References

Ding Y, Sikka DR (2006) Synoptic systems and weather. In: Wang B (ed) The Asian monsoon. pp 131–201

Gao X, Xu Y, Zhao Z, Pal JS, Giorgi F (2006) On the role of resolution and topography in the simulation of East Asian precipitation. Theor Appl Clim 86:173–185

Huffman GJ et al. (1997) The global precipitation climatology project (GPCP) combined precipitation dataset. Bull Am Meteorol Soc 78:5–20

Huffman GJ et al. (2001) Global precipitation at one-degree daily resolution from multi-satellite observations. J Hydrometeorol 2:36–50

Iguchi T, Kozu T, Meneghini R, Awaka J, Okamoto K (2000) Rain-profiling algorithm for the TRMM Precipitation Radar. J Appl Meteorol 39:2038–2052

Kamiguchi K, Kitoh A, Uchiyama T, Mizuta R, Noda A (2006) Changes in precipitation-based extremes indices due to global warming projected by a global 20-km-mesh atmospheric model. SOLA 2:64–67

Kang IS et al (2002a) Intercomparison of the climatological variations of Asian summer monsoon precipitation simulated by 10 GCMs. Clim Dyn 19:383–395

Kang IS et al (2002b) Intercomparison of atmospheric GCM simulated anomalies associated with the 1997/98 El Niño. J Clim 15:2791–2805

Kitoh A (2004) Effects of mountain uplift on East Asian summer climate investigated by a coupled atmosphere-ocean GCM. J Clim 17:783–802

Kitoh A, Arakawa O (1999) On overestimation of tropical precipitation by an atmospheric GCM with prescribed SST. Geophys Res Lett 26:2965–2968

Kobayashi C, Sugi M (2004) Impact of horizontal resolution on the simulation of the Asian summer monsoon and tropical cyclones in the JMA global model. Clim Dyn 23:165–176

Kusunoki S, Yoshimura J, Yoshimura H, Noda A, Oouchi K, Mizuta R (2006) Change of Baiu rain band in global warming projection by an atmospheric general circulation model with a 20-km grid size. J Meteorol Soc Jpn 84:581–611

Lau NC (1985) Modeling the seasonal dependence of the atmospheric response to observed El Niños in 1962–76. Mon Weather Rev 113:1970–1996

Mizuta R, Oouchi K, Yoshimura H, Noda A, Katayama K, Yukimoto S, Hosaka M, Kusunoki S, Kawai H, Nakagawa M (2006) 20-km-mesh global climate simulations using JMA-GSM model – Mean climate states–. J Meteorol Soc Jpn 84:165–185

Ninomiya K (2000) Large- and meso-a-scale characteristics of Meiyu/Baiu front associated with intense rainfalls in 1–10 July 1991. J Meteorol Soc Jpn 78:141–157

Oouchi K, Yoshimura J, Yoshimura H, Mizuta R, Kusunoki S, Noda A (2006) Tropical cyclone climatology in a global-warming climate as simulated in a 20 km-mesh global atmospheric model: frequency and wind intensity analyses. J Meteorol Soc Jpn 84:259–276

Randall D, Pan DM (1993) Implementation of the Arakawa-Schubert cumulus parameterization with a prognostic closure. Meteorol Monogr 46:145–150

Rayner NA, Parker DE, Horton EB, Folland CK, Alexander LV, Rowell DP, Kent EC, Kaplan A (2003) Global analyses of sea surface temperature, sea ice, and night marine air temperature since the late nineteenth century. J Geophys Res 108:4407, doi:10.1029/2002JD002670

Rowell DP (1998) Assessing potential seasonal predictability with an ensemble of multidecadal GCM simulations. J Clim 11:109–120

Sperber KR, Palmer TN (1996) Interannual tropical rainfall variability in general circulation model simulations associated with the Atmospheric Model Intercomparison Project. J Clim 9:2727–2750

Sugi M, Kawamura R, Sato N (1997) A study of SST-forced variability and potential predictability of seasonal mean fields using the JMA global model. J Meteorol Soc Jpn 75:717–736

Taylor KE (2001) Summarizing multiple aspects of model performance in a single diagram. J Geophys Res 106:7183–7192

Tian S-F, Yasunari T (1998) Climatological aspects and mechanism of spring persistent rains over Central China. J Meteorol Soc Jpn 76:57–71

Uchiyama T, Mizuta R, Kamiguchi K, Kitoh A, Noda A (2006) Changes in temperature-based extremes indices due to global warming projected by a global 20-km-mesh atmospheric model. SOLA 2:68–71

Ueda H, Yasunari T (1996) Maturing process of summer monsoon over the western North Pacific—a coupled ocean/atmosphere system. J Meteorol Soc Jpn 74:493–508

Ueda H, Yasunari T, Kawamura R (1995) Abrupt seasonal change of large-scale convective activity over the western Pacific in the northern summer. J Meteorol Soc Jpn 73:795–809

Uppala SM et al (2005) The ERA-40 re-analysis. Q J R Meteorol Soc 131:2961–3012

Wang B, Ding Q, Fu X, Kang IS, Jin K, Shukla J, Doblas-Reyes F (2005) Fundamental challenges in simulation and prediction of summer monsoon rainfall. Geophys Res Lett 32:L15711, doi:10.1029/2005GL022734

Wu R, Kirtman B (2005) Roles of Indian and Pacific ocean air-sea coupling in tropical atmosphere variability. Clim Dyn 25:155–170

Xie P, Arkin PA (1997) Global precipitation: A 17-year monthly analysis based on gauge observations, satellite estimates, and numerical model outputs. Bull Am Meteorol Soc 78:2539–2558

Xie SP, Xu H, Saji NH, Wang Y, Liu WT (2006) Role of narrow mountains in large-scale organization of Asian monsoon convection. J Clim 19:3420–3429

Xie P, Yatagai A, Chen M, Hayasaka T, Fukushima Y, Liu C, Yang S (2007) A gauge-based analysis of daily precipitation over East Asia. J Hydrometeorol (in press)

Yatagai A, Xie P, Kitoh A (2005) Utilization of a new gauge-based daily precipitation dataset over monsoon Asia for validation of the daily precipitation climatology simulated by the MRI/JMA 20-km-mesh AGCM. SOLA 1:193–196